A Computational Study of LEV development on Compliant 2D Wings using a Low-Fidelity FSI model

David J. Willis*
University of Massachusetts Lowell, Lowell, MA, 01854, USA.
Antonio Monteiro †
University of Massachusetts Lowell, Lowell, MA, 01854, USA.
Per Olof Persson ‡
University of California Berkeley, Berkeley, CA, 94720, USA.

This paper presents a fluid-structure interaction parameter space study focused on the development of leading edge vortices (LEVs) on two-dimensional, bio-inspired wings. The unsteady aerodynamics are computationally modeled using a linear-strength doublet lattice panel method incorporating both leading and trailing edge shedding. Two structural strategies are examined to model the bio-inspired, 2D wing structure: (a) a discrete leading edge torsional spring and (b) a non-linear, large deformation, corotational 2D FEM beam model. Each of the structural models are strongly coupled to the aerodynamics solver using a Newton method.

In the first parameter study, the impact of changing the wing leading edge compliance is examined for otherwise rigid wings (1-DOF model). This study provides insight into the importance of passive wing rotation about the wing's leading edge. The second parameter study examines the effect of a compliant 2D wing modeled as a beam. This second model provides insight into the combined effects of leading edge rotation and the chordwise wing decambering deformation. The results of these parameter sweeps illustrate that appropriately tailored leading edge as well as wing chordwise compliance can provide beneficial aerodynamics force production. Specifically, the results show that compliance has a smoothing effect on the unsteady force generation by acting as a potential energy storage mechanism. Given the low fidelity nature of the model, it is recommended that these results be further investigated using higher order computations and experiments.

I. Introduction

Insects, birds and bats possess compliant, low-mass wings that during flapping, generate passive shape changes[1–4] . The leading edge skeletal structure of most natural flyers appears to promote favorable passive aero-structural responses to unsteady flow, such as gust alleviation and peak force modulation. Furthermore, in low-Reynolds number flight, as well as during low-speed flight and maneuver, animals exploit leading edge vortices (LEV's) to augment their force production.[1,5–7] In the present study we computationally examine the impact of wing leading edge and chord-wise compliance on the development and persistence of a 2D leading edge vortex (LEV).

A better understanding of the bio-inspired flapping flight parameter space can lead to a better appreciation for natural flight, as well as a stronger foundation on which to design small, bio-inspired unmanned aerial vehicles (UAVs). In particular, understanding how to tune and modulate passive compliance can lead to structural design and control system insight.

While there appears to be beneficial outcomes from a wing's passive structural response, the parameter space is large and may present challenges for discovery using higher fidelity computational tools or exper-

*Associate Professor, Senior AIAA member
†Graduate Student, University of Massachusetts, Lowell
‡Associate Professor, Senior AIAA member

iments. Furthermore, while natural flyers exhibit passive wing deformation and LEV development, it is challenging to extract the parameter-space dependence from the complex kinematics. As a result, for this effort, we developed and used a lower fidelity fluid-structure interaction tool to examine the parameter space. Both the computational capability as well as the results from parameter space studies are of practical interest in the development of small-scale unmanned aerial vehicles.

Since the parameter space for biologically inspired wings is relatively large, we focused on a tractable, and incremental parameter study. In this effort, we start with a discrete leading edge torsional spring attached to a rigid wing structure. The stiffness of the leading edge spring is modified and the resulting forces and LEV development are observed. A second parameter study examines the introduction of full-chordwise compliance, allowing the wing surface to deform in response to the applied aerodynamics force. The computations are performed for a wing initially at rest and accelerated (with constant acceleration) to a final velocity.

II. Methods

The computational tool we present is comprised of a strongly coupled potential flow aerodynamics solver and two different structural solvers. The structural solvers examined are a simple discrete torsional spring-mass-damper and a non-linear large deformation, small strain, co-rotational FEM beam model directly following and implementing the formulation presented by Yaw.[8,9] The two structural models as well as the aerodynamics solver are described in the sections that follow.

A. Doublet Lattice Panel Method Aerodynamics Solver

A 2D linear strength doublet lattice panel method (DLPM) is used to represent the potential flow unsteady aerodynamics.[10,11] The linear doublet representation is equivalent to a constant vorticity panel method, with overall circulation implicitly included. This model represents the surface of the airfoil as an infinitely thin profile using doublet panels with linearly varying doublet strength. To change the wing chordwise shape (e.g., camber), the existing panel vertices are simply located in new positions – resulting in a simple approach to computationally handle wing deformation.

Vorticity shed from the leading and trailing edges of the DLPM is represented using free wakes, also comprising linear strength doublet panels. The strength of the newly shed doublet wake panels (vorticity) is prescribed at each timestep by applying a Kutta condition,[12] which, at the leading edge may incorporate the leading edge suction parameter, or LESP.[13,14] Because a sharp leading edge is considered in the studies performed in this paper, the leading edge shedding does not employ an LESP criteria. The unsteady evolution of the leading and trailing edge free wakes is performed using a second order predictor corrector method.[15] Figure 1 illustrates the linear strength, doublet lattice panel method aerodynamics solver.

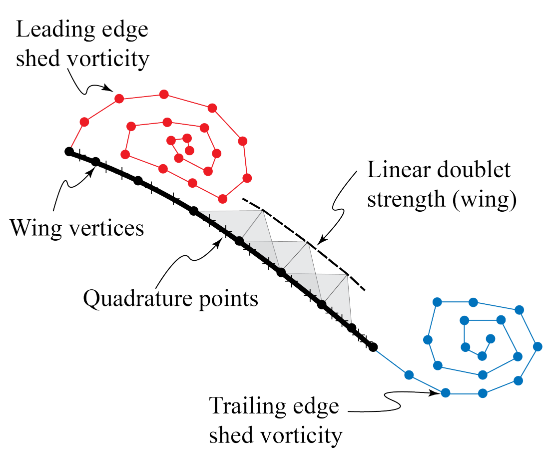

Figure 1. A graphical representation of the doublet lattice panel method aerodynamics solver.

The unsteady Bernoulli equation[12] is used to calculate the unsteady pressures on the wing at each timestep. The unsteady aerodynamics forces and moments are then determined by integrating the unsteady pressure distribution over the wing surface.

In order to detect LEV detachment from the wing, the location of the stagnation point behind the LEV may be tracked on the suction surface.[16] We used this concept and calculated the flow direction at the trailing edge to detect the timestep at which flow reversal occurs. This method for detecting LEV detachment was applied as a post-processing routine.

B. Leading Edge Torsional Spring-Mass-Damper

The simplest structural model we considered in this work was a leading edge torsional spring-mass-damper model shown in Figure 2-a. The moment balance at the leading edge can be modeled using the following equation, which permits both linear as well as non-linear springs and dampers:

$$I\frac{d^2\theta}{dt^2} + C_\theta\frac{d\theta}{dt} + k_\theta\theta + M_{aero} = 0 \tag{1}$$

This model effectively balances the unsteady aerodynamics moments at the leading edge with the spring-mass-damper dynamic system. Integrating this model with the aerodynamics model is relatively simple due to the ease by which the leading edge aerodynamic moment can be calculated.

C. Non-linear, Corotational Beam Structural Solver

A second model we use for capturing the structural deformation is a non-linear geometry, small strain, 2D beam model shown in Figure 2-b. In this model, the structure is represented using a 2D corotational finite element formulation presented by Yaw.[8,9] As such the wing compliance is represented using a chordwise compliant 2-D beam. A small *ghost* beam element is introduced ahead of the leading edge of the wing to model the effect of leading edge rotational compliance. This ghost element does not interact with the fluid domain and only serves the purpose of providing a torsional compliance at the leading edge location.

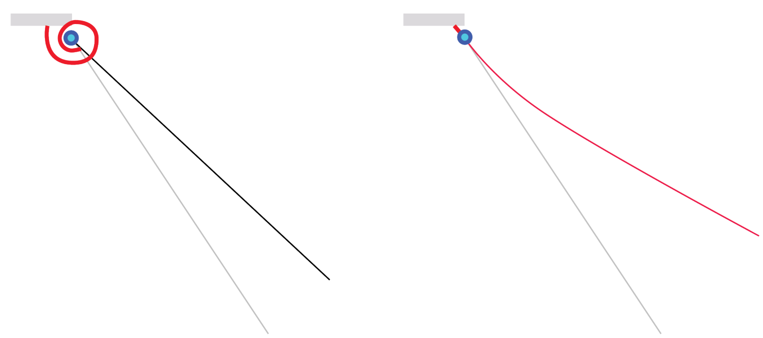

Figure 2. Schematics of the compliant wings. (left) The rigid wing with a discrete leading edge torsional spring (right) the compliant 2D beam structural model. The red color indicates compliant members for each structural strategy.

D. Fluid structure interaction coupling

The strong fluid structure interaction coupling is accomplished using a Newton/secant method solver with a numerically calculated (finite differences) Jacobian update matrix. At each timestep, the equilibrium equations are written to relate the fluid forces to the structural deformation. A force/moment residual expression is minimized at each coupling iteration to ensure the aerodynamics forces and structure are in equilibrium. This residual minimization typically requires 10-30 steps per time-step.

For coupling the corotational beam formulation, the number of finite elements in the beam model was less than the number of surface elements used in the aerodynamics computation. This disparity in the number of elements was leveraged to reduce the number of unknowns in the coupling equations and reduce the size of the Jacobian matrix. As a result, the aerodynamics forces were interpolated to the nodes of the structural model using the concept of equivalent forces and moments. The structural beam deformation was likewise interpolated using a cubic spline to generate a smooth curve to represent the airfoil mid-line and the new locations of the aerodynamics nodes and elements. The result was a markedly lower computational cost for the fluid dynamics components of the Jacobian matrix. Despite this lower cost, the Jacobian matrix was often calculated and reused for multiple FSI iterations until the efficiency of the Newton method suffered. This resulted in an efficient, and approximate Newton method which had reasonably good performance.

III. Computational Cases and Structure Parameter Space Description

Two different parameter spaces are explored in this paper:

1. A discrete leading edge torsional spring structural model
2. A 2D beam structure with a ghost element at the leading edge.

These parameter space studies are presented in the sections below.

1. Discrete leading edge compliance, rigid wing

In this parameter study, only the leading edge torsional spring stiffness is examined. The damping and mass are assumed to be negligible and are therefore assigned a value of zero. The stiffness of the leading edge is varied between a very compliant spring ($K_\theta = 0.100$) and a very stiff spring ($K_\theta = 2.000$) in twenty increments. This structural parameter space was examined for initial wing incidence angles of $\alpha = 60, 45, 30$ degrees. Table 1 summarizes these case parameters.

Table 1. The parameters used for the rigid wing with a discrete leading edge spring.

	L.E. Spring Constant, N-m/rad per unit span	Wing	**Initial Angle** deg.
Exp. 1a	k = 0.100, 0.200, 0.300, ... , 2.000	Rigid	60 deg.
Exp. 1b	k = 0.100, 0.200, 0.300, ... , 2.000	Rigid	45 deg.
Exp. 1c	k = 0.100, 0.200, 0.300, ... , 2.000	Rigid	30 deg.

2. Leading edge compliance, with a continuously compliant wing

In this parameter study, we varied both the leading edge and the wing compliance. To do this, we modified the stiffness of the beam (Stiffness = $\frac{EI}{A}$). The stiffness of the leading edge was varied in a logarithmic manner and the main wing beam was varied in a linear manner. In total, 120 different structural combinations were defined. These differently compliant wings described weak-leading edges with weak-beams through to stiff leading edges and stiff beams. The compliant wings were modeled with initial angles of 30, 45 and 60 degrees incidence. A summary of the parameters is presented in table 2.

Table 2. The parameters used with the continuously compliant beam and leading edge ghost node.

	Leading Edge Stiffness $\frac{EI}{A}$	**Beam Stiffness** $\frac{EI}{A}$	**Initial Angle** deg.
Exp. 2a	2.5e-5, 5e-5, 1.25e-4, 2.50e-4, 5.0e-4, 1.25e-3, 2.5e-3, 5e-3, 0.0125, 0.0250, 0.050, 0.125	0.00125, 0.00250, 0.00375,... 0.01250	60 deg.
Exp. 2a	2.5e-5, 5e-5, 1.25e-4, 2.50e-4, 5.0e-4, 1.25e-3, 2.5e-3, 5e-3, 0.0125, 0.0250, 0.050, 0.125	0.00125, 0.00250, 0.00375,... 0.01250	45deg.
Exp. 2a	2.5e-5, 5e-5, 1.25e-4, 2.50e-4, 5.0e-4, 1.25e-3, 2.5e-3, 5e-3, 0.0125, 0.0250, 0.050, 0.125	0.00125, 0.00250, 0.00375,... 0.01250	30 deg.

A. Experimental Case Description

The computational experiments examine wings undergoing a start-up process with prescribed startup kinematics matching those presented by Manar et al[17,18] . For each of the test cases, the wings and fluid are initially at rest. At $t^* = 0$, ($t^* = U \cdot t/c$, where the velocity, $U = 0.26$ m/s and the chord, $c = 0.0762$) the wings start to accelerate with a constant acceleration, such that the distance travelled during the acceleration phase is $s/c = 2.0$. The wings reach a final velocity of $U = 0.26 m/s$ which is held constant until the unsteady simulation is over (t^* 6). Overall, the wing acceleration is completed after a non-dimensional time, $t^* \simeq 4.0$. Once the wings reach the steady state velocity, the cases are run until approximately $t^* \simeq 6.0$. For our low-fidelity model, each simulation comprised 80 computational timesteps.

IV. Computational Results and Discussion

In this section, computational results are presented for each of the different experimental cases, along with a brief discussion of the salient points.

1. Computational Results and Discussion: Discrete Leading Edge Spring - High Order CFD Comparisons

The low-order results for cases with a leading edge spring (60-degree initial angle) are first compared with computations that are performed using 3DG[19] , a high-order, Discontinuous Galerkin method for solving the Navier Stokes equations. For these comparisons, the wing kinematics (i.e., the wing angle) from the low-order fluid-structure interaction are used as inputs into the 3DG solver. This is done to allow comparisons of the flow-field development for similar kinematics (and not the fluid structure interaction).

The time dependent normal, lift and drag force coefficients are presented in figure 3. These results show that for the acceleration phase of the computational experiment ($t^* < 4.0$), the low- and high-fidelity solutions compare quite favorably. The high-fidelity flow predictions exhibit slightly higher force coefficient production predictions than the low fidelity results during this portion of the cases. Furthermore, the differences between the methods are both amplified and less trend based after the wing has completed its acceleration phase ($t^* > 4.0$). This is likely due to the wing kinematics (incidence angle) from the low-fidelity solver being more strongly dependent on the specific unsteady fluid dynamics forces. If both the low- and high-fidelity cases both considered the fluid structure interaction, there may be better or at least trend based agreement.

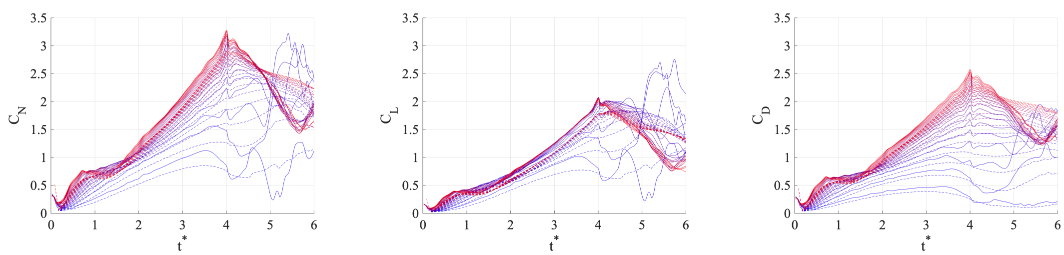

a) Normal Force Coefficient b) Lift Coefficient c) Drag Coefficient

Figure 3. The fluid structure interaction response for rigid wings with discrete leading edge compliance initially set at 60 degrees incidence – results using high order CFD are presented as solid lines, whereas, the results for the low-order CFD re dashed lines. The spring constant varies from very compliant (blue) to stiff (red).

A flowfield comparison of both the low- and high-fidelity solutions is presented for leading edge springs, $k = 0.1$ through $k = 1.8$ N-m/rad per span. These comparisons show the low-fidelity solution plotted as an overlay on the post-processed high fidelity results images for approximately the same timestep, $t^* \approx 4.0$. While this overlay is not numerically/temporally exact, the comparison does show promising agreement for all but the most compliant springs ($k = 0.1$ N-m/rad per span and $k = 0.2$ N-m/rad per span). These highly compliant springs tend to create shallow angles to the flow compared with the less compliant springs – resulting in flows that are likely more sensitive to LEV viscous interaction with the upper surface of the wing. It is also likely that viscous effects such as boundary layer growth/displacement not considered in the potential flow solver may have a larger impact in these cases where the LEV is weaker.

2. Computational Results and Discussion: Discrete Leading Edge Spring

The discrete leading edge spring model simulations are presented in Figures 5 through 7. The results presented here include the time-varying force coefficients, geometry (wing angle) as well as the total shed leading edge and trailing edge (wake) circulation. The results are shown for each of the cases with colors varying from blue (cases with the most compliant leading edge) to red (cases with the least compliant leading edge). The plots also show the results for fixed incidence angle, rigid wings using gray reference lines (ranging from 15 degrees to 60 degrees in five degree increments). These fixed incidence angle, rigid wings are provided as a non-compliant baseline comparison.

The results in Figures 5 through 7 show clear leading edge compliance trends. As expected, we observe that stiffer wings tend to have results that trend closer to the rigid wings. The more compliant springs tend to result in greater wing deflection/rotation (Figures 5 through 7 -b) which in turn results in lower force production (Figures 5 through 7 - a, c, d) and less total leading edge circulation (Figures 5 through 7 -f) and trailing edge wake circulation (Figures 5 through 7 -g). Interestingly, we see that wings with greater compliance also exhibit greater lift to drag ratios (Figures 5 through 7 -e)– this is primarily due to the wing rotation about the leading edge allowing the wing normal force to contribute more to lift generation than drag generation.

Comparing results in Figures 5,6 and 7, we can also observe that the greater the wing incidence angle, the greater the LE and TE total circulation and the greater the normal force coefficient. The force coefficients (Figures 5 through 7 -a, c) also exhibit force peaks at later times as the wing incidence is decreased, whether by lower initial angle or lower compliance.

The force coefficient results (Figures 5 through 7 -a,c,d) illustrate how compliant wings tend to modulate or smooth unsteady forces for the case. For example, all of the fixed incidence angle rigid wings exhibit a sudden force peak at $t^* = 4.0$ corresponding to the end of the wing start-up acceleration phase. The wing acceleration changes at this point in time from a constant to zero acceleration – the result of this deceleration is account for by the unsteady Bernoulli equation as a sudden reduction in the unsteady pressure. Conversely, for compliant wings, the force coefficients all show smoother responses at this time, due primarily to the small adjustments that the leading edge spring is able to make in the pitch angle in response to this change in the wing kinematics. Effectively, the stored potential energy in the leading edge spring is harnessed along with the acceleration of flow around the airfoil to mitigate the unsteady reduction in forces. This exchange of potential energy between the spring and the surrounding fluid has a favorable effect on maintaining smoother force production with respect to time.

In addition to the unsteady force modulation effect, the compliant wings also exhibit a more gradual loss of lift than the fixed-rigid counterparts. This beneficial and interesting outcome can likely be partially attributed to the compliant wings' return to the original undeformed state as the leading edge moment (and normal force) declines (as seen in Figures 5 through 7 -b). This *spring-back* effect is analogous to a potential energy storage device or fluid-structural battery, in which the structure absorbs energy during the aerodynamic loading process and returns the energy to the flow during the loss of force generation. Overall, we anticipate this fluid-structural coupling would be beneficial to practical flight situations.

3. Computational Results and Discussion: Continuous Beam Model

The continuous beam model simulations are presented in Figures 8 through 28. The results are first separated by initial wing incidence angle (60, 45, and 30 degrees respectively). The results are then further separated into parameters (force coefficients, wing LE-TE angle, lift-to-drag ratio and LE/TE circulation) and finally into a series of plots showing the structural influences of the leading edge and airfoil-beam structure (6 figures each with 12 sub-plots). Following the presentation of the detailed results, a summary containing six contour plots presents the value of the parameters at the peak force generation point. For each of the detailed plots, the results for each leading edge compliance value are presented in a single plot with varying wing compliance shown in blue (case with most compliance) to red (case with least compliance) wings. The overall collection of results represents 120 different wing structural configurations each modeled at 3 different initial incidence angles for a total of 360 FSI simulations.

The results illustrate that the combination of leading edge compliance and overall wing compliance can be effectively used to tailor a desired aerodynamics outcome. When wings have a very compliant beam structure and a compliant leading edge, the wing angular deformation is significant and the resulting forces and circulation production are low, and high angular deformations are observed. The converse is also true, a stiff leading edge combined with a stiff wing beam results in greater force production and greater leading edge vortex circulation. In cases where a compliant wing beam is coupled with a stiff leading edge element (or visa versa), a range of intermediate forces and circulation generation is observed. Correspondingly, these combinations of different leading edge and beam stiffnesses are the ones that produce the most variation in angular response. In extreme cases, the wing or leading edge compliance may dominate and the resulting wing does not exhibit significant differences from similar cases (eg. a low leading edge stiffness shows similar results regardless of the wing beam stiffness).

The force generation results exhibit similar trends as the discrete leading edge spring cases discussed in the previous section, and are presented below in detail:

- **Wing Angle:** The wing angle is reported using a line connecting the leading edge to the trailing edge. While this measure neglects wing camber, the result can provide some insight into the wing deformation. From the results in figures 9, 16 and 23 -a,b,c the angular deformation of a wing is most pronounced when the leading edge has excessive compliance. Similarly, an overly compliant wing beam (Figures 9, 16 and 23 -all plots, blue lines) will dominate the wing angular deflection response. It is only when there is sufficient stiffness in both the leading edge element and the wing beam that there is a diversity of response, most notable in Figures 9, 16 and 23 - e through l. This varied angular response provides insight into which wing structures are likely to be effective for different situations – but is overall as would be expected.

- **Force and Circulation production:** The more compliant wings tend to produce lower lift (normal and drag) forces and subsequently exhibit less circulation generation as seen in Figures 8, 15, 22 - a,b,c. This is an expected result of the introduction of compliance as the wing will tend to deform to alleviate the aerodynamics force generation. The results in Figures 10, 17, and 24 also show that the introduction of wing or leading edge compliance absorbs the sudden changes in the force coefficients, resulting in relatively smoother force generation time histories. This is observed most prominently at $t^* = 4.0$ when the acceleration due to wing start-up suddenly changes. For very compliant wings (a,b,c and blue lines on subsequent plots), the fluctuations of force coefficients are smooth and are related to the unsteady components of the case (initial acceleration, and the interaction of the wing with the shed vorticity in the LEV). Overall, compliant wings when compared with rigid wings at similar angles to the flow tend to change shape to attenuate force peaks.

- **Post-force-peak behavior:** The compliant beam-wing results in Figures 8, 10, 15, 17, 22, and 24 also show that certain compliant wings (those that are less compliant) have favorable force behavior post-peak force coefficient value. These compliant wings exhibit a gradual loss of lift and normal force compared with their non-compliant counterparts which have a faster drop-off in the force production. It was also noted that the non-dimensional time corresponding to the peak force coefficient is not coincident with the detachment/separation of the LEV. As such, it may be that compliance is a useful property to reduce the unsteady loads associated with LEV detachment. This behavior is valuable from a vehicle design standpoint as it suggests that compliant wings produce a less abrupt loss of lift after the peak force is achieved. It is hypothesized that this gradual loss of lift and normal force is related to the compliant wing *springing-back* towards its undeformed state once the peak force has been reached. During this *spring-back*, the stored deformation energy is recovered and and used to influence the flow. The tailing edge in these cases tends to translate more than any other location along the wing chord – resulting in both shed vorticity at the trailing edge as well as unsteady normal and lift forces.

- **Lift-to-drag ratio:** The lift-to-drag ratio results for compliant wings shown in Figures 12,19, and 26 again illustrate that compliant wings tend to benefit from re-orienting the lifting surface and thus the overall force vector forward to produce more lift and less drag. This however, does come at the expense of lower overall lift forces. This ultimately raises the possibility that a rigid wing could achieve the same favorable result by actively adjusting the wing angle.

- **Effect of wing stiffness on LEV detatchment:** Figure 29 illustrates the predicted non-dimensional time at which LEV detatchment occurs for the 60 degree beam-wing when using a trailing edge flow reversal criteria to predict LEV separation. The results indicate that the beam stiffness has a considerable impact on the LEV persistence, with non-dimensional time increasing by approximately 25% as the wing stiffness is varied from very compliant to stiff. Similarly, there is an LEV detachment delay as the leading edge stiffness is increased. These results suggest that LEV persistence on flexible wings is greater when the wings are stiffer and remain closer to the undeformed state. This said, it should be noted that the LEV detachment from compliant wings does not correspond to the peak lift force generation in this study – and that perhaps compliant wings may possess a favorable fore generation behavior despite the detatchment of the LEV. This is a result that should be further investigated using higher fidelity computational tools.

V. Conclusions

The fluid structure interaction of two different strategies for compliant 2D wings was examined using a low-fidelity doublet lattice method computational tool. The low-fidelity computational tool is shown to have reasonable agreement with higher order CFD for both the time dependent forces and in the comparison of flow fields for times $t^* < 4.0$. For times greater than $t^* = 4.0$ further study and results comparison using high fidelity FSI tools is recommended.

The wing structural strategies that were examined include (1) a rigid flat plate with a compliant leading edge modeled as a torsional spring and (2) a chordwise compliant wing that uses a beam to model the wing. The results showed the following:

1. Greater structural compliance tends to reduce the force production capacity of the wings due to load alleviation shape changes.
2. Structural compliance tends to smooth the development of unsteady forces by allowing small shape changes to absorb sudden unsteady force generation.
3. Structural compliance appears to provide an elastic potential energy storage mechanism. As forces rise, the deformation of the structure absorbs some of the system energy, and as forces decline, the structure tends to return or *spring back* to its original undeformed state. During this *spring back* phase, the change in aerodynamics forces is predicted to be more gradual than non-compliant wings. This result should be examined further using high fidelity tools, since this effect is observed for times $t^* > 4.0$.
4. Wings with more structural compliance appear to result in earlier detachment of the LEV from the wing than those wings with less compliance. Despite the earlier detatchment of the LEV, the force coefficient generation is not significantly impacted by this, infact, the structural compliance appears to have a positive effect on generating a more gradual loss of forces. This result also should be further investigated using higher fidelity tools.

While the low-fielity tool is an effective means to cost-effectively exploring the structural parameter space, the use of a higher fidelity tool to confirm the overall trends observed is recommended.

VI. Acknowledgements

This material is based upon work supported by the National Science Foundation under Grants No. 1511507. Any opinions, findings, and conclusions or recommendations expressed in this material are those of the author(s) and do not necessarily reflect the views of the National Science Foundation.

References

[1]Kang, C.-K. & Shyy, W. (2012). Passive Wing Rotation in Flexible Flapping Wing Aerodynamics. 30th AIAA Applied Aerodynamics Conference 2012. 10.2514/6.2012-2763.

[2]Swartz, S. M. (1997). Allometric patterning in the limb skeleton of bats: implications for the mechanics and energetics of powered flight. Journal of Morphology, 234(3), 277-294.

[3]Von Busse, R., Hedenstrm, A., Winter, Y., & Johansson, L. C. (2012). Kinematics and wing shape across flight speed in the bat, Leptonycteris yerbabuenae. Biology open, 1(12), 1226-1238.

[4]Sullivan, T. N., Wang, B., Espinosa, H. D., & Meyers, M. A. (2017). Extreme lightweight structures: avian feathers and bones. Materials Today, 20(7), 377-391.

[5]Hubel, T. Y., & Tropea, C. (2010). The importance of leading edge vortices under simplified flapping flight conditions at the size scale of birds. Journal of Experimental Biology, 213(11), 1930-1939.

[6]Ellington, C. P., Van Den Berg, C., Willmott, A. P., & Thomas, A. L. (1996). Leading-edge vortices in insect flight. Nature, 384(6610), 626-630.

[7]Videler, J. J., Stamhuis, E. J., & Povel, G. D. E. (2004). Leading-edge vortex lifts swifts. Science, 306(5703), 1960-1962.

[8]M. A. Crisfield. Non-linear Finite Element Analysis of Solids and Structures - Vol 1. John Wiley & Sons Ltd., Chichester, England, 1991.

[9]Louie L. Yaw, 2D Corotational Beam Formulation, Walla Walla University, November 30, 2009. `https://gab.wallawalla.edu/~louie.yaw/Co-rotational_docs/2Dcorot_beam.pdf`

[10]Willis, D. J., Anwar, M.I., Gowda, R.B.V., Manar, F. & Jones, A.R. (2018). An Unsteady Doublet Lattice Method for Studying LEV Development on Low-Re Wings with Leading Edge Compliance with Experimental Comparison. AIAA 2018-0312, In 31st AIAA Scitech Conference, 2018.

[11]Monteiro, A., Vail, K. M., Persson, P. O., Jones, A. R., & Willis, D. J. (2020). A Computational Study of the Impact of Fluid Structure Interaction on the Development and Persistence of 2D LEVs in Low Reynolds Number Flow Applications. In AIAA AVIATION 2020 FORUM (p. 2689).

[12]Katz, J., & Plotkin, A. (2001). Low-speed aerodynamics (Vol. 13). Cambridge university press.

[13]Ramesh, K., Gopalarathnam, A., Ol, M. V., Granlund, K., & Edwards, J. R. (2011). Augmentation of inviscid airfoil theory to predict and model 2d unsteady vortex dominated flows. AIAA Paper, 3578, 2011.

[14]Ramesh, K., Gopalarathnam, A., Edwards, J. R., Ol, M. V., & Granlund, K. (2013). An unsteady airfoil theory applied to pitching motions validated against experiment and computation. Theoretical and Computational Fluid Dynamics, 27(6), 843-864.

[15]Butcher, J. C. (1987). The numerical analysis of ordinary differential equations: Runge-Kutta and general linear methods. Wiley-Interscience.

[16]Rival, D. E., Kriegseis, J., Schaub, P., Widmann, A., & Tropea, C. (2014). Characteristic length scales for vortex detachment on plunging profiles with varying leading-edge geometry. Experiments in fluids, 55(1), 1-8.

[17]Manar, F., & Jones, A. R. (2017). Transient response of a single degree-of-freedom wing at high angle-of-attack. AIAA Journal, 3681-3692.

[18]Manar, F., & Jones, A. R. (2019). Evaluation of potential flow models for unsteady separated flow with respect to experimental data. Physical Review Fluids, 4(3), 034702.

[19]Persson, P.-O., Willis, D.J. & Peraire, J. (2012), Numerical simulation of flapping wings using a panel method and a high-order Navier-Stokes solver. Int. J. Numer. Meth. Engng, 89: 12961316. doi:10.1002/nme.3288

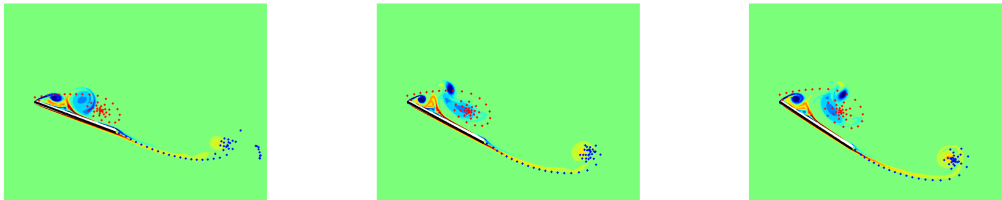

a) k = 0.1 N-m/rad per span b) k = 0.2 N-m/rad per span c) k = 0.3 N-m/rad per span

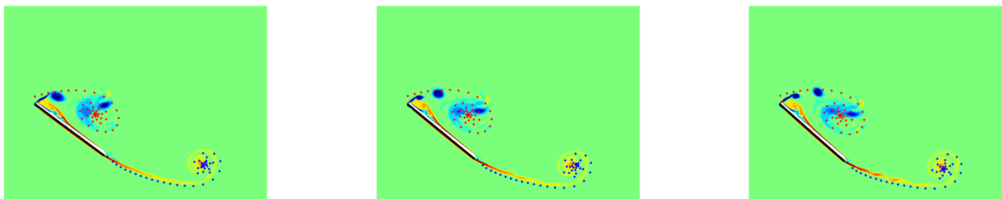

d) k = 0.4 N-m/rad per span e) k = 0.5 N-m/rad per span f) k = 0.6 N-m/rad per span

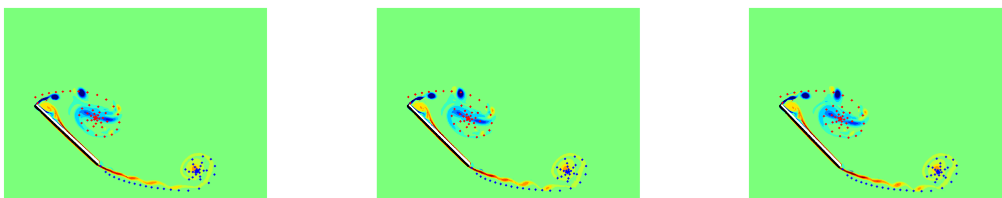

g) k = 0.7 N-m/rad per span h) k = 0.8 N-m/rad per span i) k = 0.9 N-m/rad per span

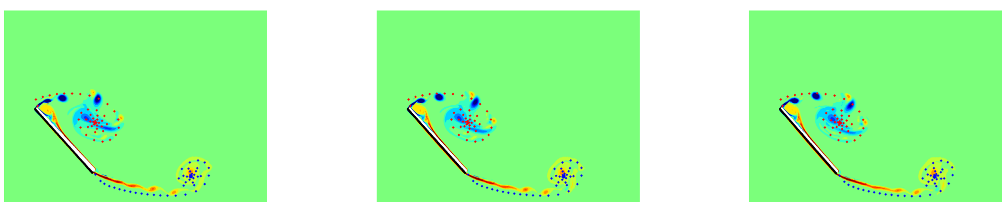

d) k = 1.0 N-m/rad per span e) k = 1.1 N-m/rad per span f) k = 1.2 N-m/rad per span

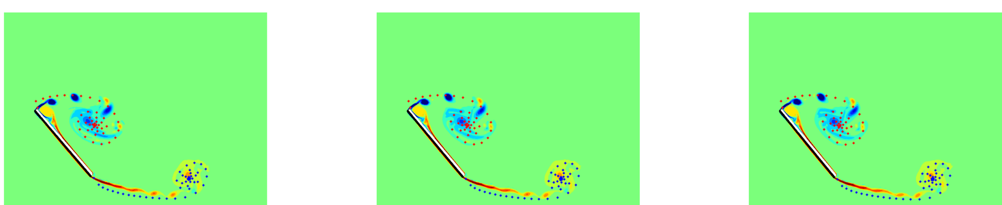

d) k = 1.3 N-m/rad per span e) k = 1.4 N-m/rad per span f) k = 1.5 N-m/rad per span

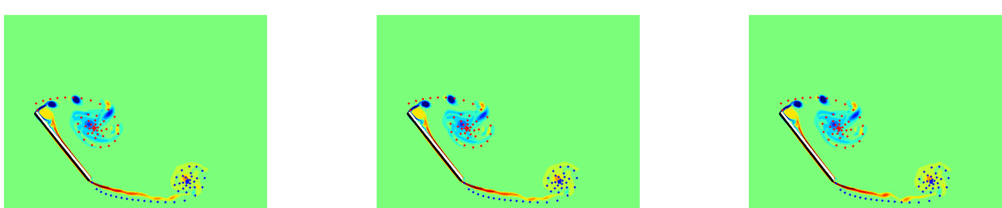

d) k = 1.6 N-m/rad per span e) k = 1.7 N-m/rad per span f) k = 1.8 N-m/rad per span

Figure 4. The low-order doublet lattice panel method result is overlaid on the high order CFD flow output image results at the nearest equivalent timestep at t^* 4.0. These results are presented for k = 0.1 - k = 1.8 N-m/rad per span

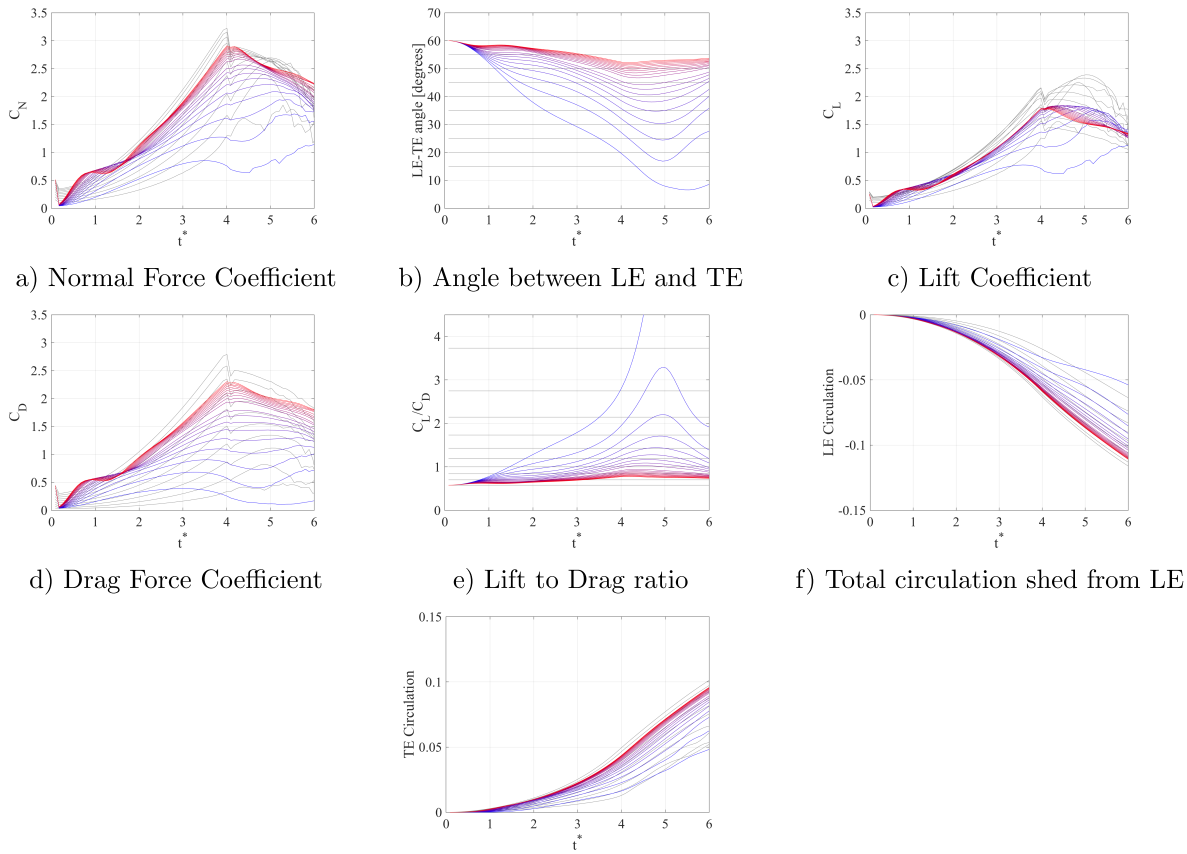

a) Normal Force Coefficient

b) Angle between LE and TE

c) Lift Coefficient

d) Drag Force Coefficient

e) Lift to Drag ratio

f) Total circulation shed from LE

g)Total circulation shed from TE

Figure 5. The fluid structure interaction response for rigid wings with discrete leading edge compliance initially set at 60 degrees incidence. The spring constant varies from very compliant (blue) to stiff (red).

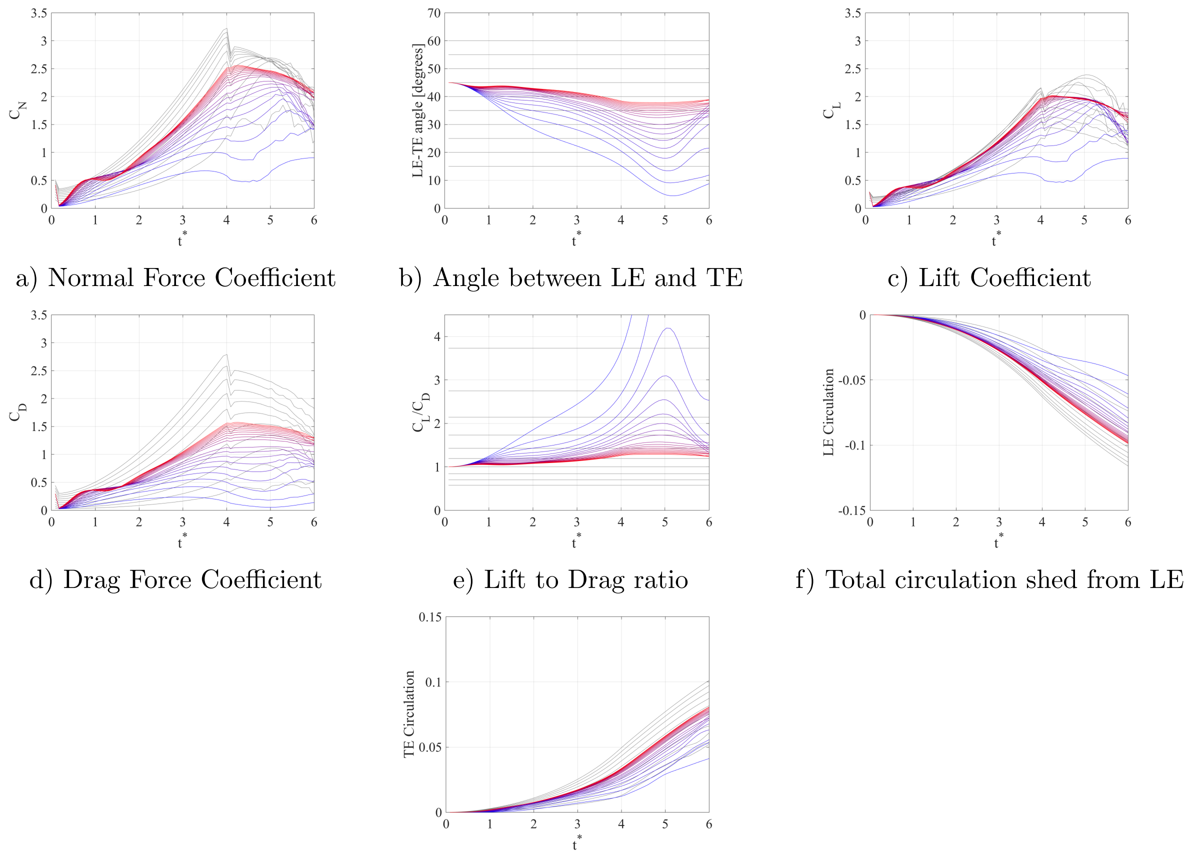

a) Normal Force Coefficient
b) Angle between LE and TE
c) Lift Coefficient
d) Drag Force Coefficient
e) Lift to Drag ratio
f) Total circulation shed from LE
g)Total circulation shed from TE

Figure 6. The fluid structure interaction response for rigid wings with discrete leading edge compliance initially set at 45 degrees incidence. The spring constant varies from very compliant (blue) to stiff (red).

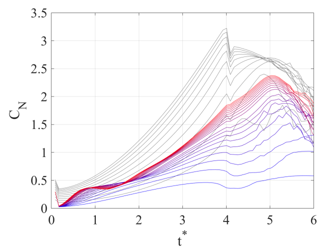

a) Normal Force Coefficient

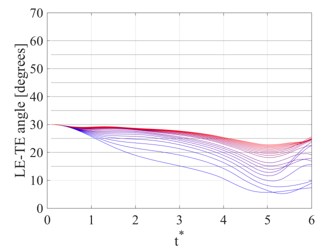

b) Angle between LE and TE

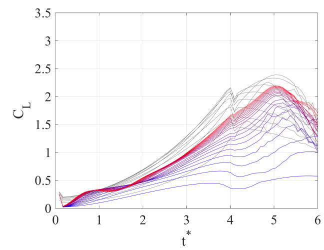

c) Lift Coefficient

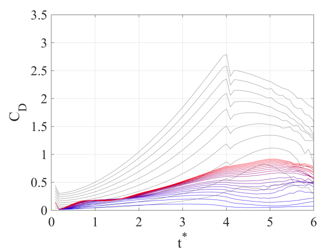

d) Drag Force Coefficient

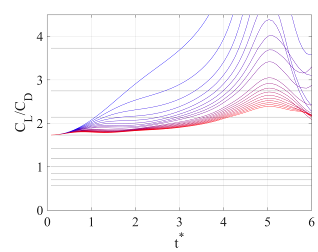

e) Lift to Drag ratio

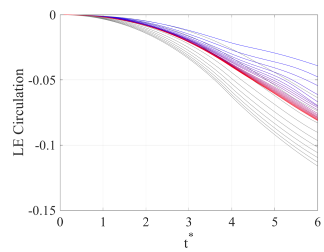

f) Total circulation shed from LE

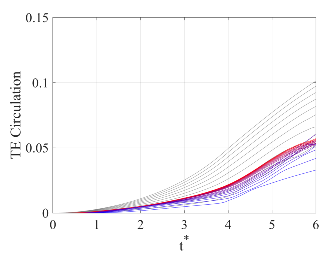

g)Total circulation shed from TE

Figure 7. The fluid structure interaction response for rigid wings with discrete leading edge compliance initially set at 30 degrees incidence. The spring constant varies from very compliant (blue) to stiff (red).

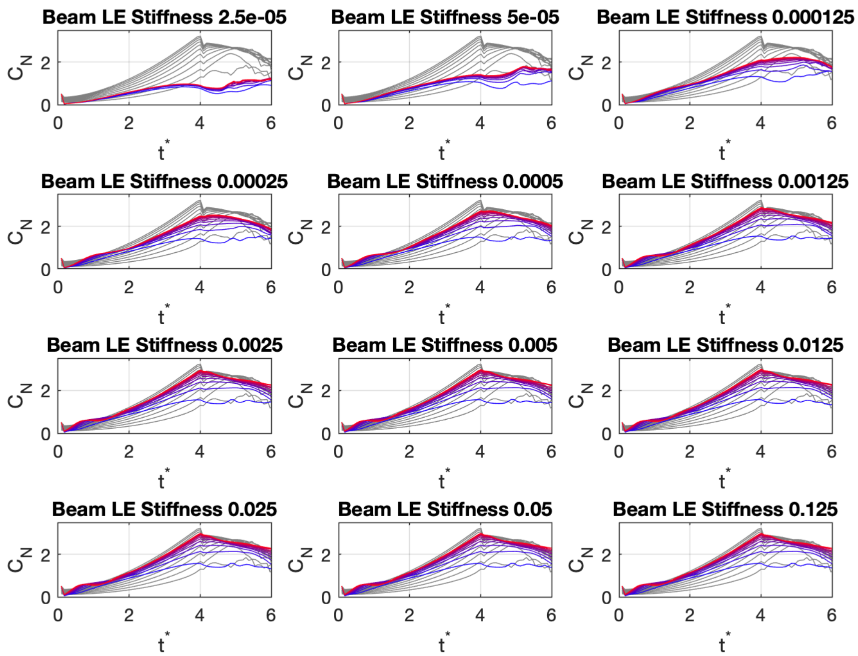

Figure 8. Normal Force Coefficient, 60 deg. initial incidence

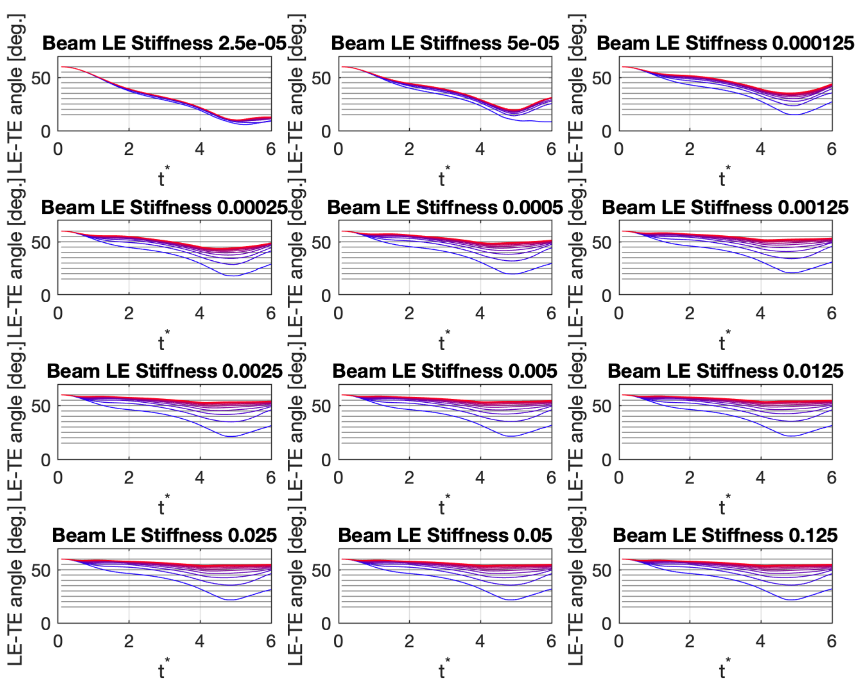

Figure 9. Angle between leading and trailing edge, 60 deg. initial incidence

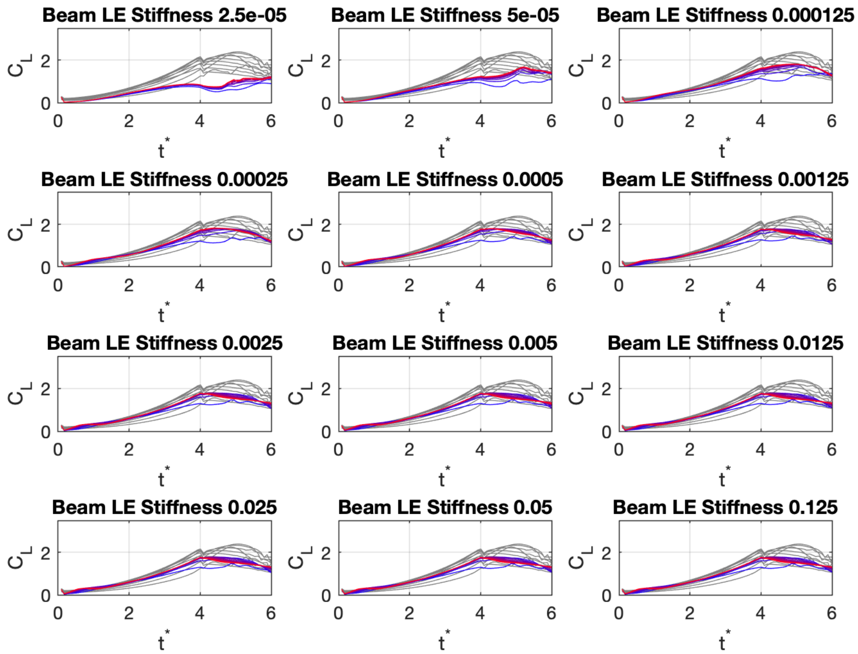

Figure 10. Lift Force Coefficient, 60 deg. initial incidence

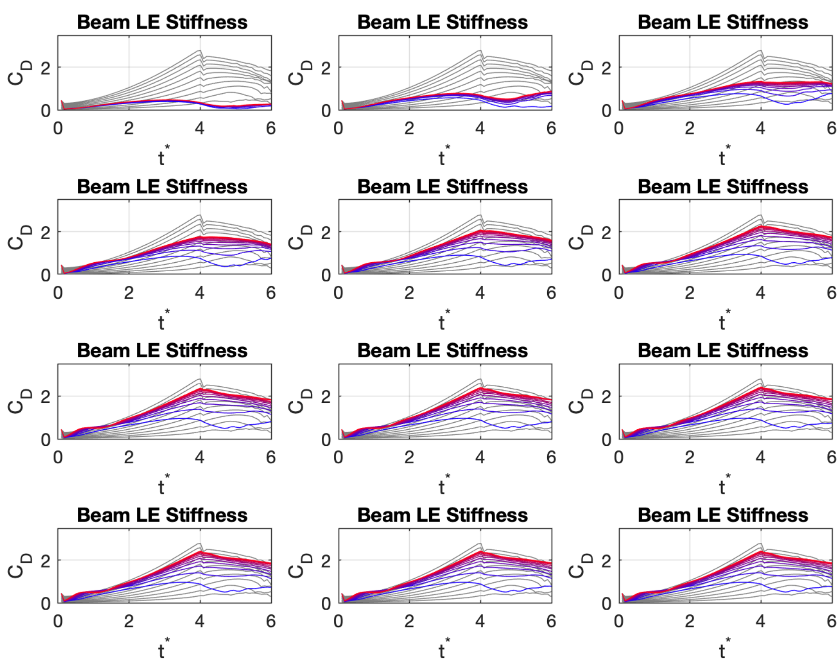

Figure 11. Drag Force Coefficient, 60 deg. initial incidence

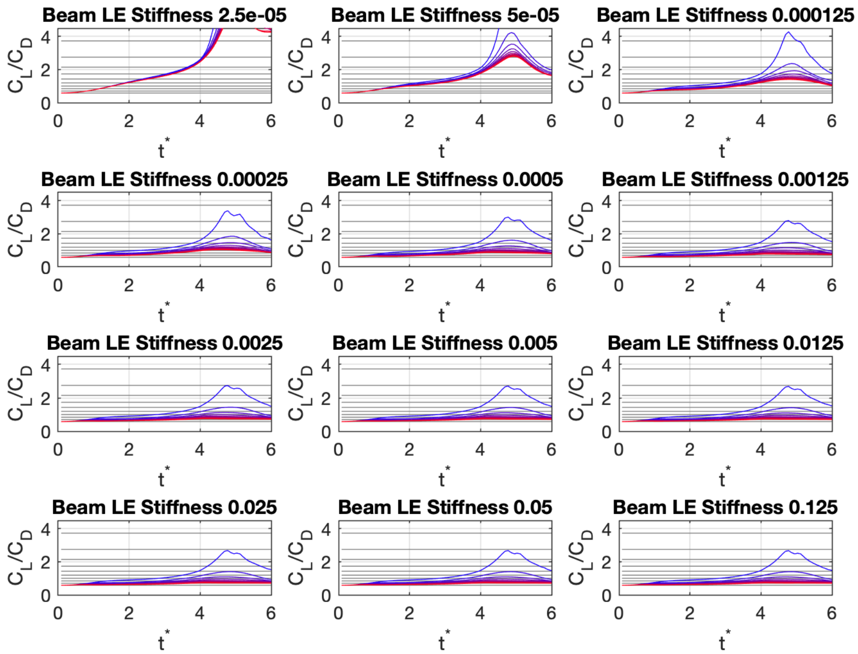

Figure 12. Lift to Drag Ratio, 60 deg. initial incidence

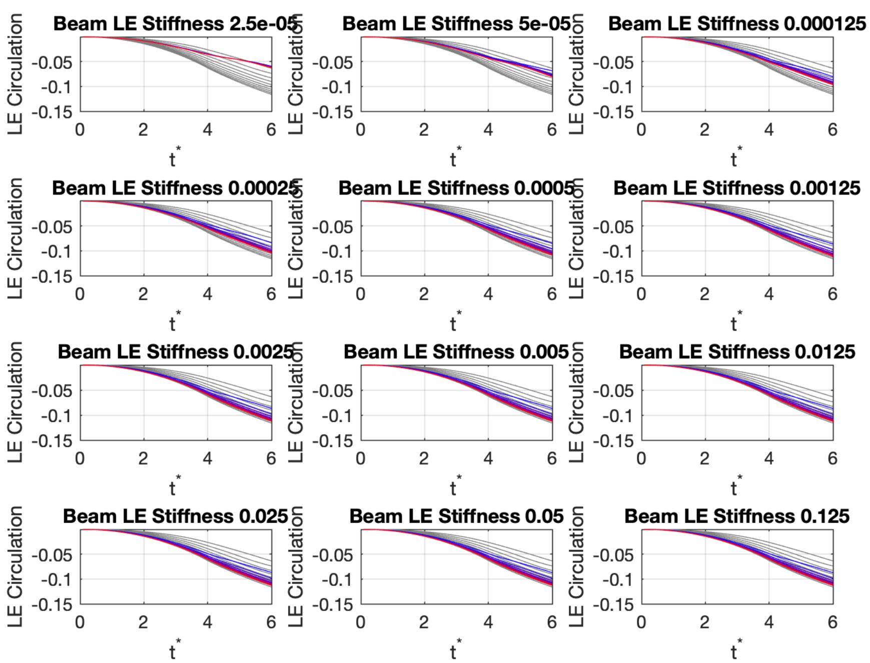

Figure 13. LE Circulation, 60 deg. initial incidence

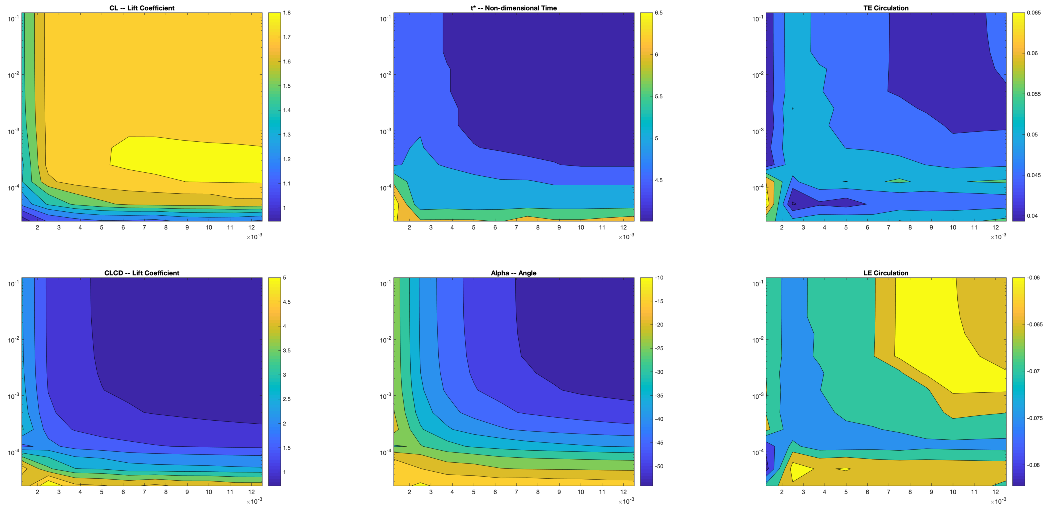

Figure 14. A parameter space for compliant 2D wings initially at 60 degrees incidence. The plots show the values of the force coefficients and vortex structure total circulation at the time (t^*) associated with the peak normal force coefficient value in the given situation. The x-axis shows the wing beam compliance while the y-axis shows the wing leading edge compliance.

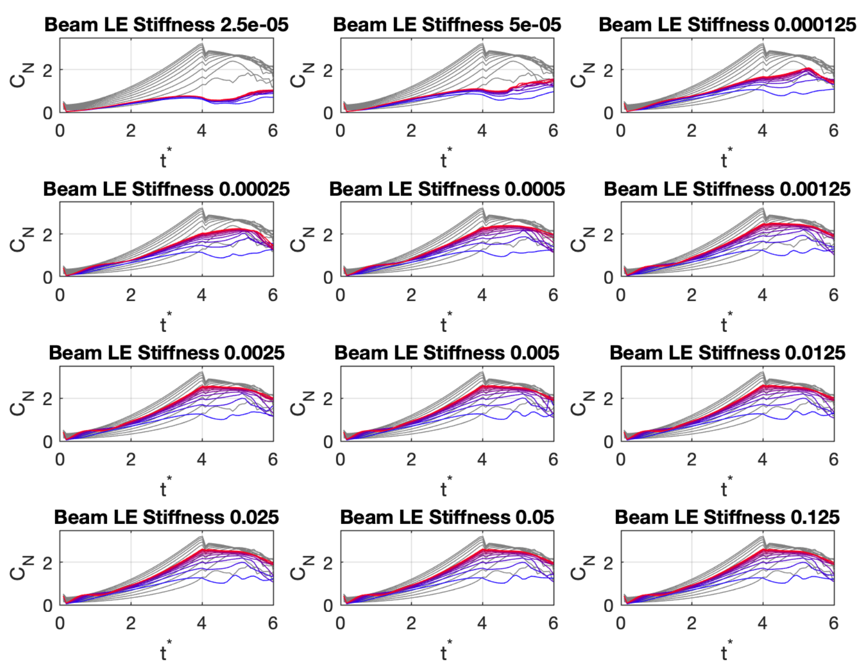

Figure 15. Normal Force Coefficient, 45 deg. initial incidence

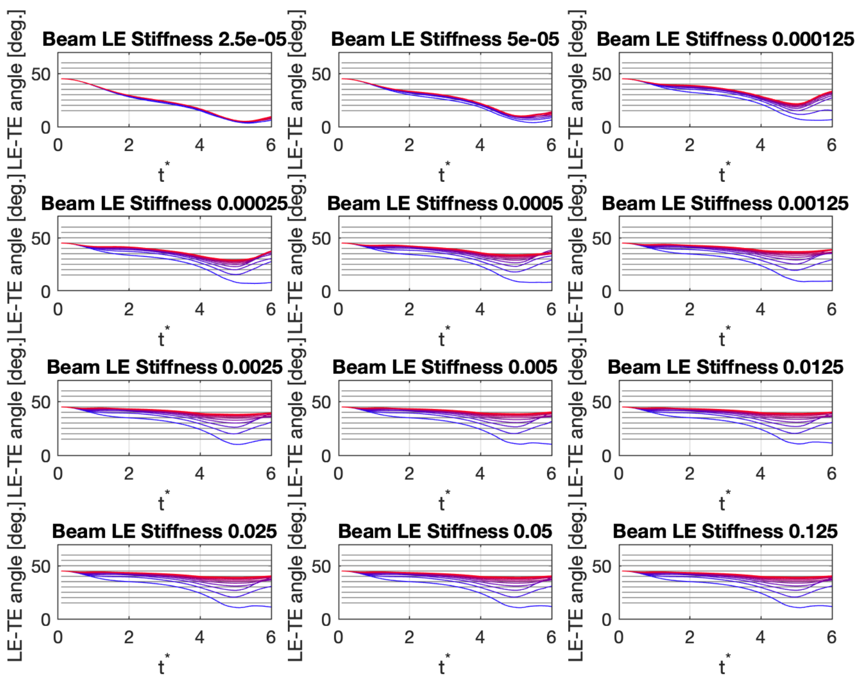

Figure 16. Angle between leading and trailing edge, 45 deg. initial incidence

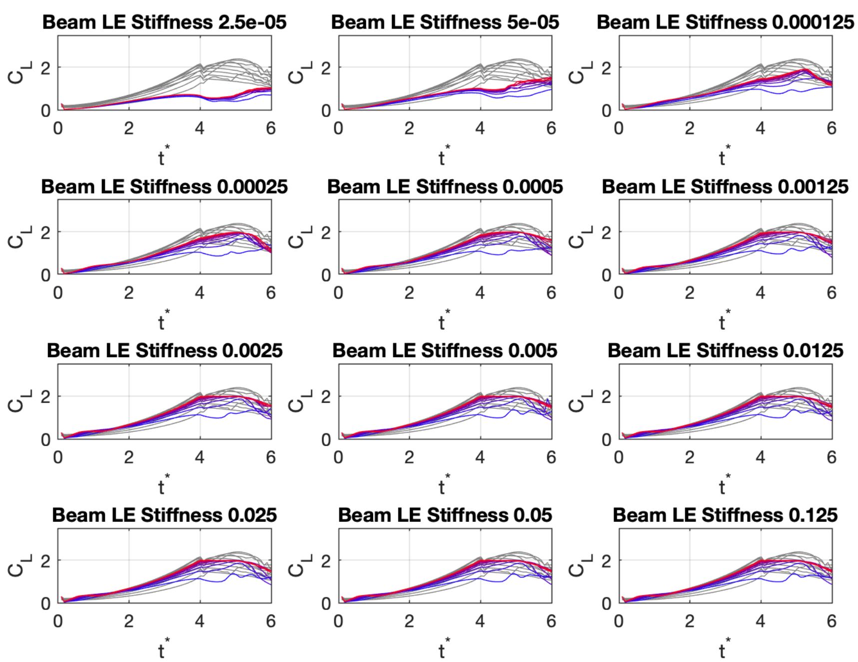

Figure 17. Lift Force Coefficient, 45 deg. initial incidence

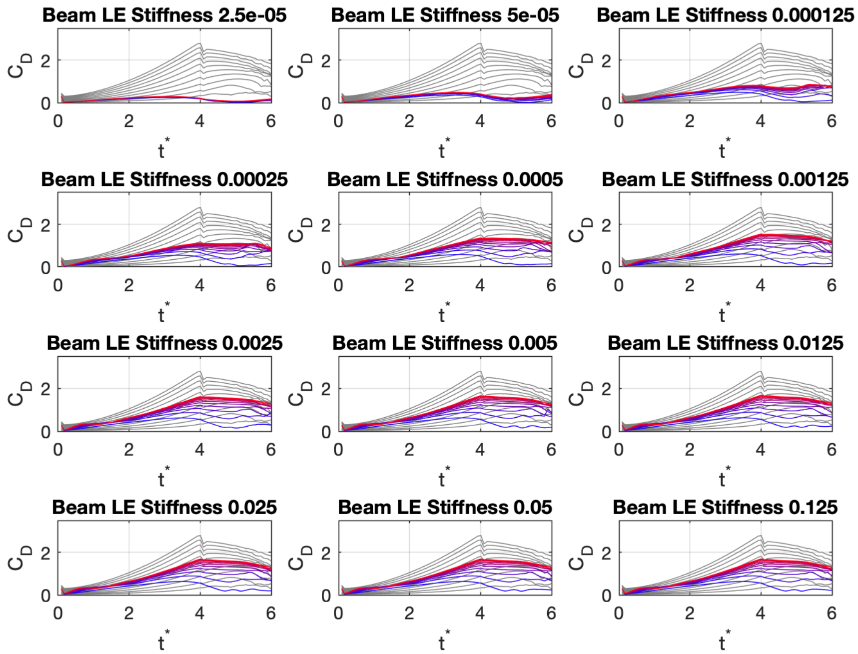

Figure 18. Drag Force Coefficient, 45 deg. initial incidence

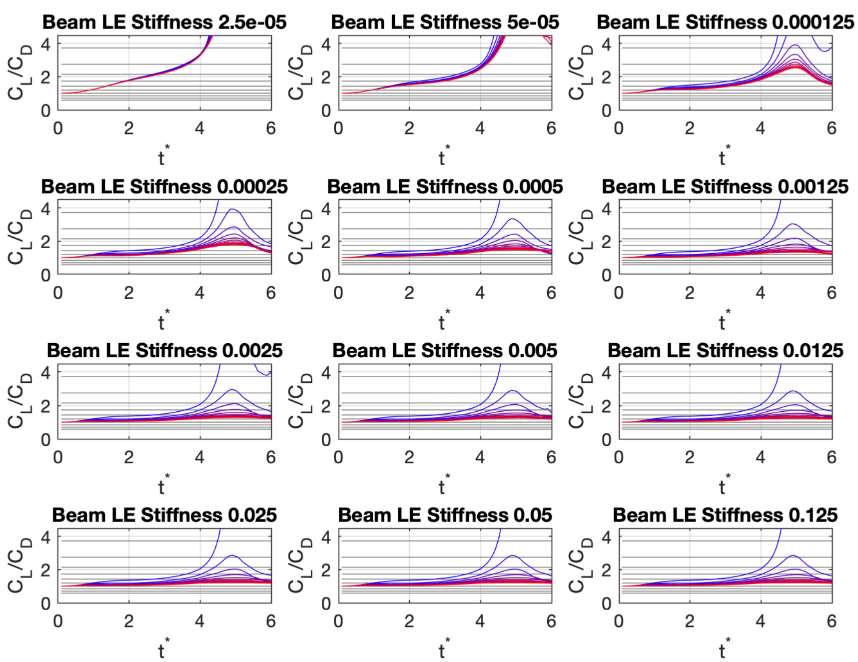

Figure 19. Lift to Drag Ratio, 45 deg. initial incidence

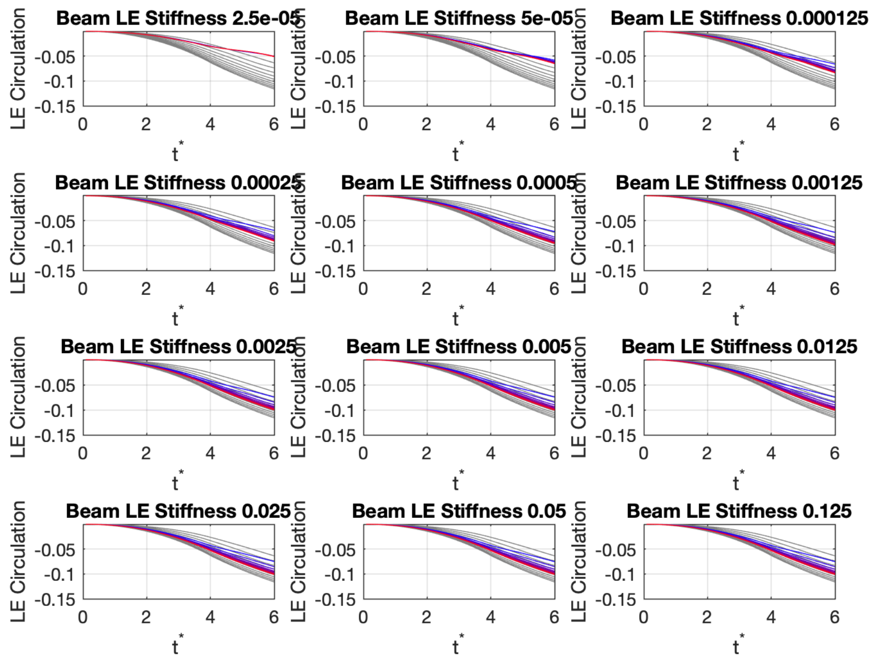

Figure 20. LE Circulation, 45 deg. initial incidence

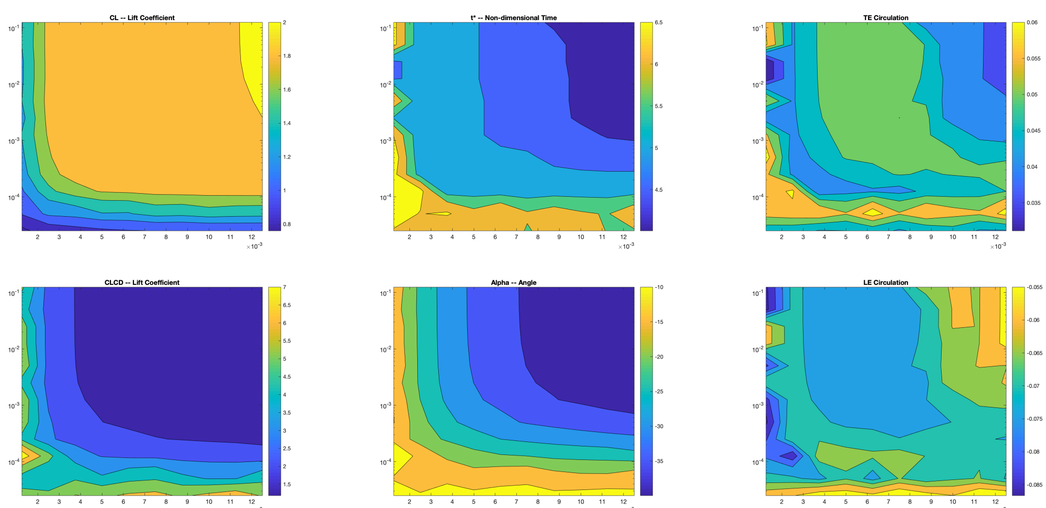

Figure 21. A parameter space for compliant 2D wings initially at 45 degrees incidence. The plots show the values of the force coefficients and vortex structure total circulation at the time (t^*) associated with the peak normal force coefficient value in the given situation. The x-axis shows the wing beam compliance while the y-axis shows the wing leading edge compliance.

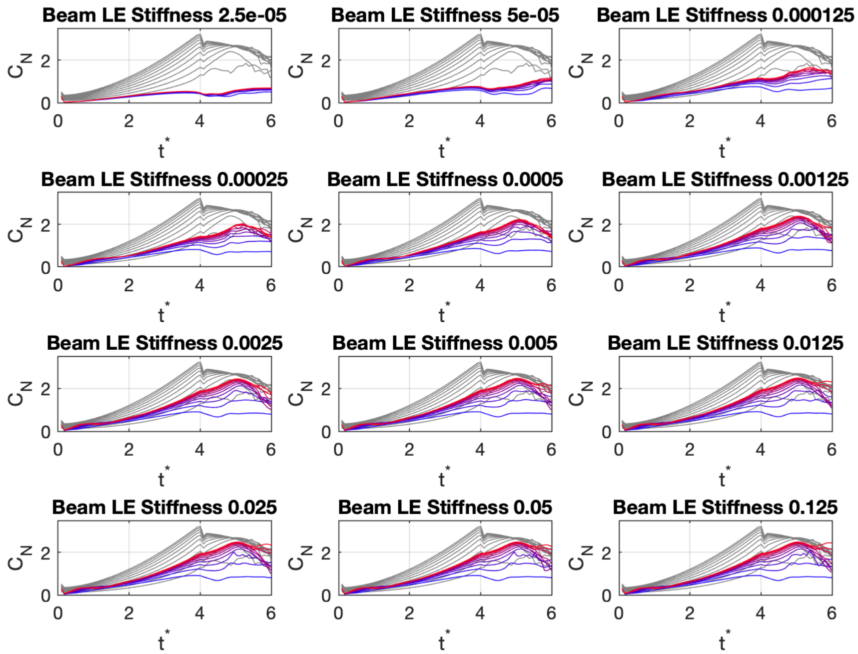

Figure 22. Normal Force Coefficient, 30 deg. initial incidence

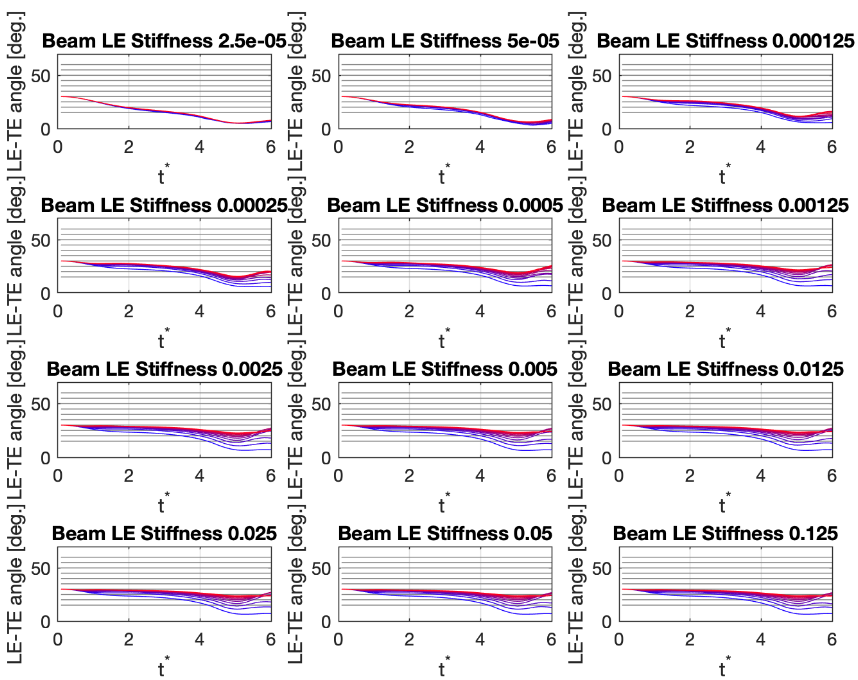

Figure 23. Angle between leading and trailing edge, 30 deg. initial incidence

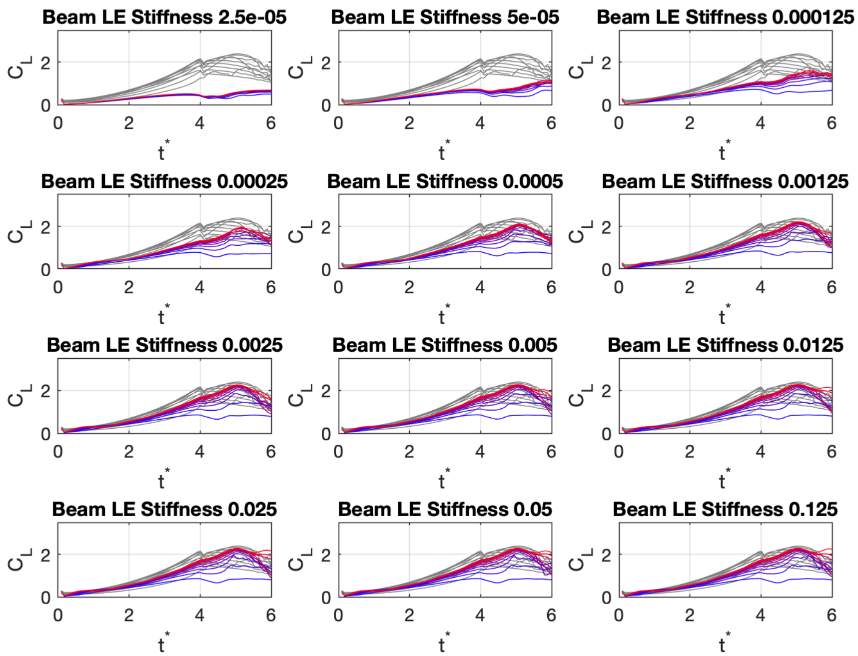

Figure 24. Lift Force Coefficient, 30 deg. initial incidence

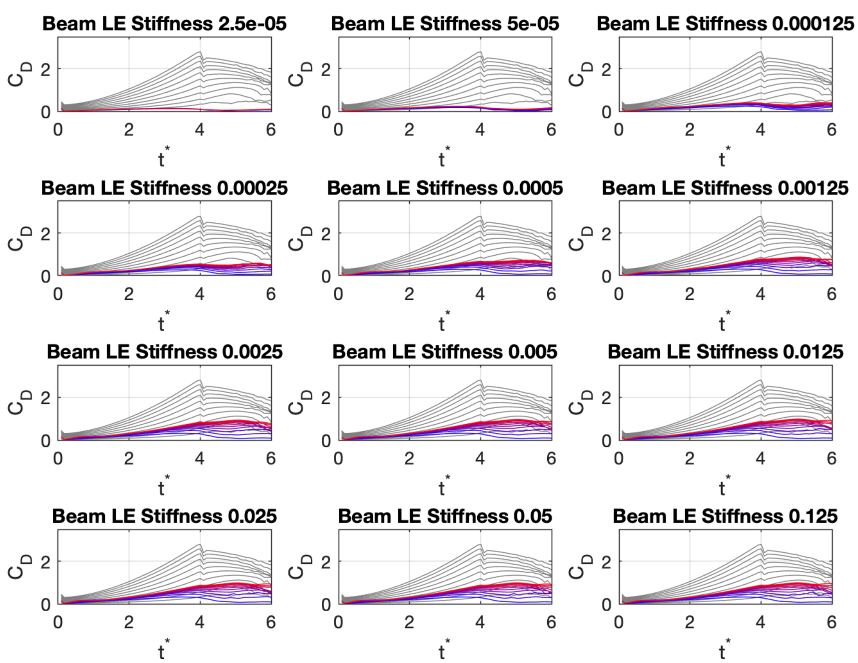

Figure 25. Drag Force Coefficient, 30 deg. initial incidence

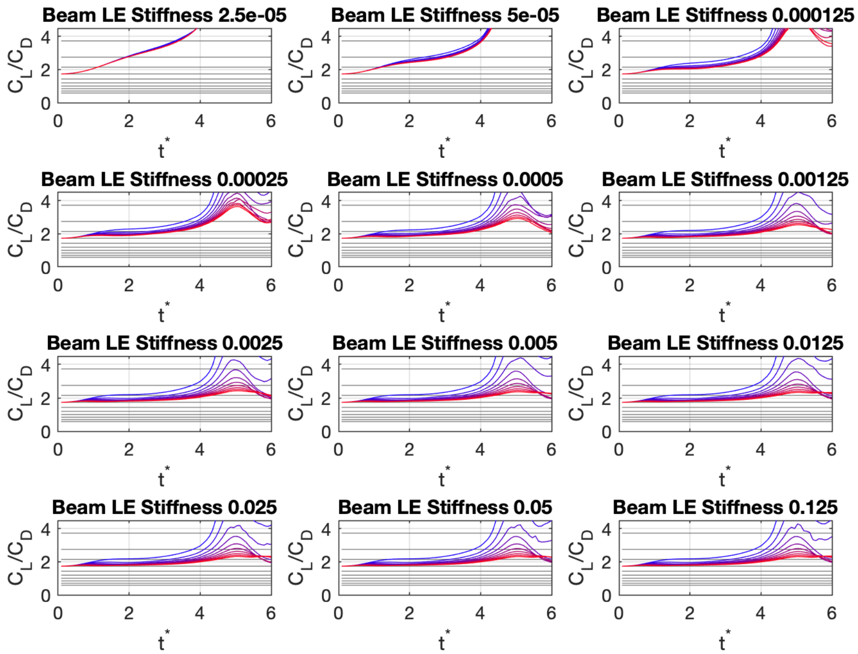

Figure 26. Lift to Drag Ratio, 30 deg. initial incidence

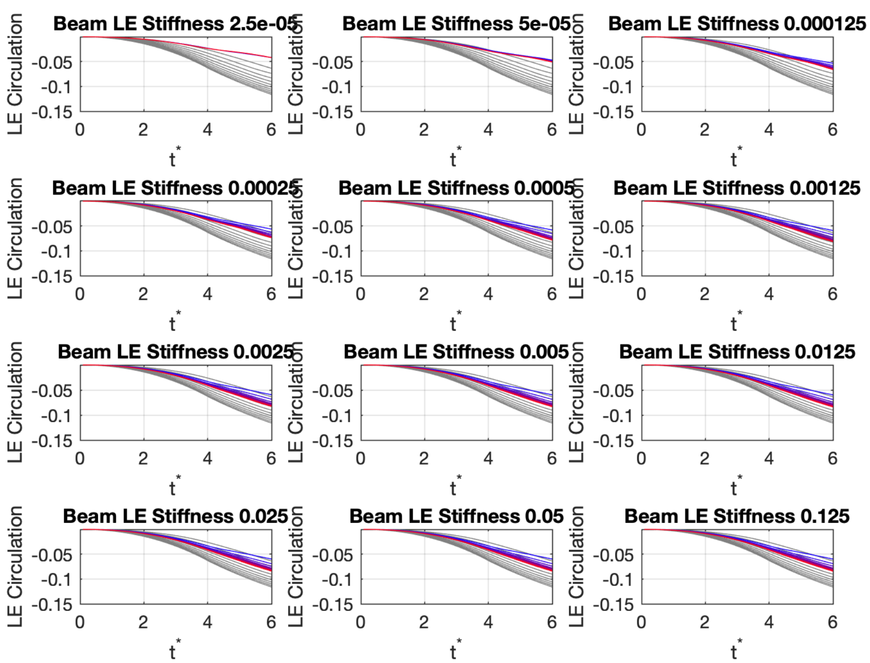

Figure 27. LE Circulation, 30 deg. initial incidence

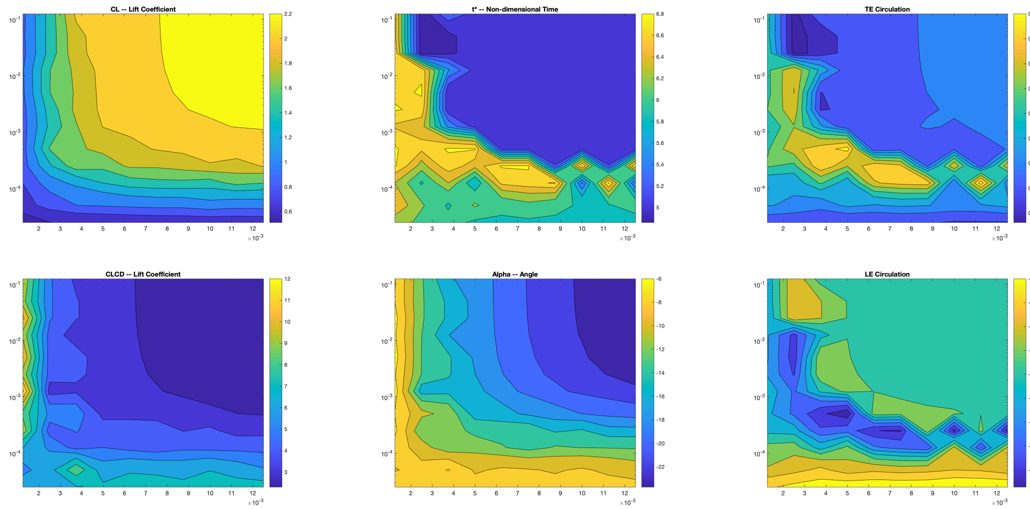

Figure 28. A parameter space for compliant 2D wings initially at 30 degrees incidence. The plots show the values of the force coefficients and vortex structure total circulation at the time (t^*) associated with the peak normal force coefficient value in the given situation. The x-axis shows the wing beam compliance while the y-axis shows the wing leading edge compliance.

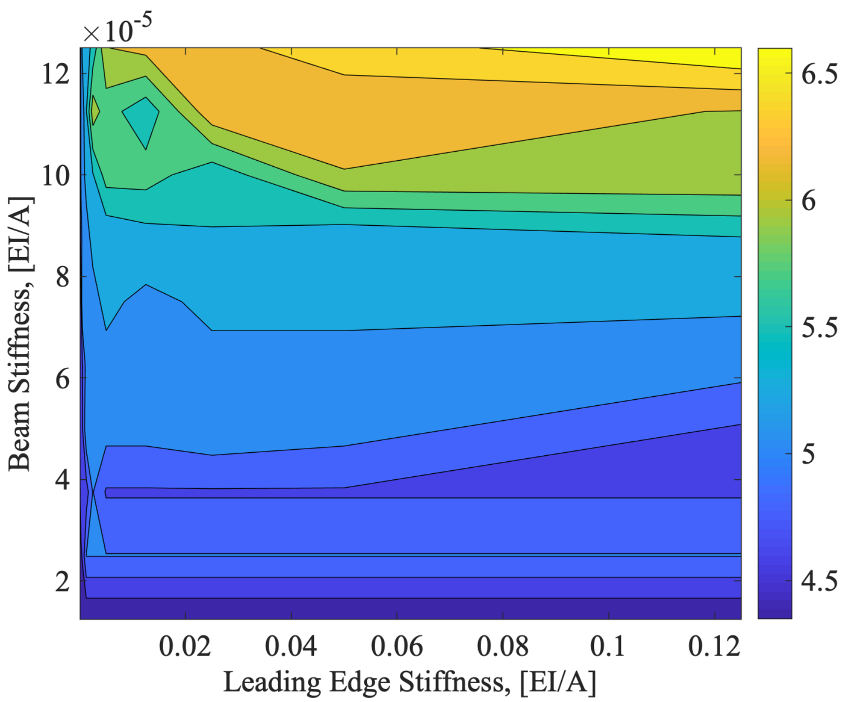

Figure 29. The predicted detachment timestep using the trailing edge flow reversal criteria. .